

AD-A253 688



PL-TR-92-2133

DTIC
ELECTE
JUL 15 1992
S C D

(2)

AN EMPIRICAL MODEL OF FUV AURORAL INTENSITY

Moshe Tur
Israel Oznovich

Tel Aviv University/Ramot Ltd
Faculty of Engineering, Ramat Aviv
Tel Aviv, 69978, ISRAEL

25 February 1992

Final Report
March 1990-February 1992

APPROVED FOR PUBLIC RELEASE; DISTRIBUTION UNLIMITED



PHILLIPS LABORATORY
AIR FORCE SYSTEMS COMMAND
HANSCOM AIR FORCE BASE, MASSACHUSETTS 01731-5000

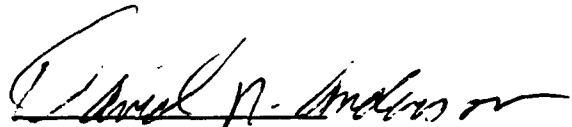
92-18395



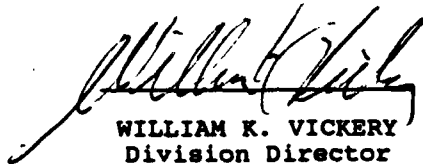
This technical report has been reviewed and is approved for publication.



FRANCIS DELGRECO
Contract Manager



DAVID ANDERSON
Branch chief



WILLIAM K. VICKERY
Division Director

This document has been reviewed by the ESD Public Affairs Office (PA) and is releasable to the National Technical Information Service (NTIS).

Qualified requestors may obtain additional copies from the Defense Technical Information Center.

If your address has changed, or if you wish to be removed from the mailing list, or if the addressee is no longer employed by your organization, please notify PL/TSI, Hanscom AFB, MA 01731-5000. This will assist us in maintaining a current mailing list.

Do not return copies of this report unless contractual obligations or notices on a specified document requires that it be returned.

REPORT DOCUMENTATION PAGE			Form Approved OMB No. 0704-0188	
<small>Public reporting burden for this collection of information is estimated to average 1 hour per response, including the time for reviewing instructions, searching existing data sources, gathering and maintaining the data needed, and completing and reviewing the collection of information. Send comments regarding this burden estimate or any other aspect of this collection of information, including suggestions for reducing this burden, to Washington Headquarters Services, Directorate for Information Operations and Reports, 1215 Jefferson Davis Highway, Suite 1204, Arlington, VA 22202-4302, and to the Office of Management and Budget, Paperwork Reduction Project (0704-0188), Washington, DC 20503.</small>				
1. AGENCY USE ONLY (Leave blank)	2. REPORT DATE 25 February 1992	3. REPORT TYPE AND DATES COVERED Final Report (March 1990-Feb 1992)		
4. TITLE AND SUBTITLE An Empirical Model of FUV Auroral Intensity		5. FUNDING NUMBERS Contract F49620-90-C-0018 PE 62101F PR 4643 TA 11 WU AL		
6. AUTHOR(S) Moshe Tur Israel Oznovich				
7. PERFORMING ORGANIZATION NAME(S) AND ADDRESS(ES) Tel Aviv University/Ramot Ltd Faculty of Engineering, Ramat Aviv Tel Aviv, 69978, ISRAEL		8. PERFORMING ORGANIZATION REPORT NUMBER		
9. SPONSORING/MONITORING AGENCY NAME(S) AND ADDRESS(ES) Phillips Laboratory Hanscom AFB, MA 01731-5000 Contract Manager: Frank DelGreco/GPIM		10. SPONSORING/MONITORING AGENCY REPORT NUMBER PL-TR-92-2133		
11. SUPPLEMENTARY NOTES				
12a. DISTRIBUTION / AVAILABILITY STATEMENT		12b. DISTRIBUTION CODE		
13. ABSTRACT (Maximum 200 words) A statistical model of auroral intensity as a function of magnetic activity was created. The model was derived from several hundred 1356Å images of the aurora borealis obtained by Polar BEAR at solar minimum. Intensities were averaged in 35 divisions of CGL (from 55° to 90°, each division 1° long), 48 divisions of MLT (each division half an hour wide), and 5 divisions of magnetic activity ($K_p = 0-4$). The peak oval intensity is located near midnight for all K_p values but 0. Two secondary maxima in the average 1356Å intensity are found in the dayside part of the oval: one in the morning and one in the afternoon.				
14. SUBJECT TERMS Aurora Ultraviolet Image processing		Polar BEAR satellite Electron precipitation		15. NUMBER OF PAGES 36
17. SECURITY CLASSIFICATION OF REPORT Unclassified		18. SECURITY CLASSIFICATION OF THIS PAGE Unclassified	19. SECURITY CLASSIFICATION OF ABSTRACT Unclassified	16. PRICE CODE
				20. LIMITATION OF ABSTRACT SAR

The peak nightside, morning, and afternoon intensity increase monotonically with magnetic activity. The latitude of peak emission increases with K_p at night and decreases in the dayside. The latitudinal extent of the oval is largest at or near the intensity peaks and increases with magnetic activity. The model of average auroral intensity was related to a statistical model of electron precipitation into the high-latitude ionosphere. The precipitation data leading to auroral emissions show a power law relationship between the energy flux and the average energy of the precipitating electrons. The average electron energy associated with the peak 1356Å oval emission is 0.8–1.7 keV at night, predominantly 0.3–0.7 keV in the morning, and predominantly 0.2–0.5 keV in the afternoon. Polar cap emissions are associated with very cold electrons (0.3–0.4 keV). The electron energy flux associated with the peak oval emission increases with magnetic activity in the morning and afternoon, but remains approximately constant (below $0.5 \text{ ergs cm}^{-2} \text{ s}^{-1}$) in the nightside for all K_p values but 2. At increasing levels of magnetic activity, the peak nightside (dayside) intensity shifts poleward (equatorward) and the peak energy flux shifts equatorward (equatorward). Energy fluxes associated with polar cap emissions are very low ($\sim 0.1 \text{ ergs cm}^{-2} \text{ s}^{-1}$). Weak 1356Å emissions (0.3–0.4 kR) at CGL 78–80°, 1200 MLT, coincide with the minimum average electron energy and maximum electron number flux associated with cusp precipitation. These emissions are located at the so-called "midday gap", which was termed as such by less sensitive imaging studies of the aurora.

Contents

1	ABSTRACT	1
2	INTRODUCTION	2
3	INSTRUMENTATION	4
4	DATA ANALYSIS	6
4.1	Image Processing	7
4.2	Binning and Smoothing of the Data	8
4.3	Electron Precipitation Maps	11
5	MAPS OF AVERAGE AURORAL INTENSITY	13
5.1	Nightside Auroral Oval	17
5.2	Dayside Auroral Oval	19
5.3	Polar Cap and Cusp	21
6	DISCUSSION AND CONCLUSIONS	23
7	SUMMARY AND FUTURE DIRECTIONS	26
8	REFERENCES	28

Accession For	
NTIS Grant	<input checked="" type="checkbox"/>
NTIS TAB	<input type="checkbox"/>
Unannounced	<input type="checkbox"/>
Justification	
By _____	
Distribution/	
Availability Codes	
Dist	Avail and/or Special
A-1	

1 ABSTRACT

A statistical model of auroral intensity as a function of magnetic activity was created. The model was derived from several hundred 1356Å images of the aurora borealis obtained by Polar BEAR at solar minimum. Intensities were averaged in 35 divisions of CGL (from 55° to 90°, each division 1° long), 48 divisions of MLT (each division half an hour wide), and 5 divisions of magnetic activity ($K_p = 0-4$). The peak oval intensity is located near midnight for all K_p values but 0. Two secondary maxima in the average 1356Å intensity are found in the dayside part of the oval: one in the morning and one in the afternoon. The peak nightside, morning, and afternoon intensity increase monotonically with magnetic activity. The latitude of peak emission increases with K_p at night and decreases in the dayside. The latitudinal extent of the oval is largest at or near the intensity peaks and increases with magnetic activity. The model of average auroral intensity was related to a statistical model of electron precipitation into the high-latitude ionosphere. The precipitation data leading to auroral emissions show a power law relationship between the energy flux and the average energy of the precipitating electrons. The average electron energy associated with the peak 1356Å oval emission is 0.8–1.7 keV at night, predominantly 0.3–0.7 keV in the morning, and predominantly 0.2–0.5 keV in the afternoon. Polar cap emissions are associated with very cold electrons (0.3–0.4 keV). The electron energy flux associated with the peak oval emission increases with magnetic activity in the morning and afternoon, but remains approximately constant (below $0.5 \text{ ergs cm}^{-2} \text{ s}^{-1}$) in the nightside for all K_p values but 2. At increasing levels of magnetic activity, the peak nightside (dayside) intensity shifts poleward (equatorward) and the peak energy flux shifts equatorward (equatorward). Energy fluxes associated with polar cap emissions are very low ($\sim 0.1 \text{ ergs cm}^{-2} \text{ s}^{-1}$). Weak 1356Å emissions (0.3–0.4 kR) at CGL 78–80°, 1200 MLT, coincide with the minimum average electron energy and maximum electron number flux

associated with cusp precipitation. These emissions are located at the so-called "midday gap", which was termed as such by less sensitive imaging studies of the aurora.

2 INTRODUCTION

Current imaging instruments afford global studies of the aurora with good spatial resolution (25–100 km). These allow one to create global maps of auroral emission and relate them to particle precipitation. A global model of the aurora can aspire to either one of two attributes: temporal accuracy that is limited to a short time interval and given magnetic conditions, or high magnetic activity resolution and coverage that is valid on the average for long time intervals, but practically void of short-time accuracy. The first approach is applied to test cases, the second on a large data set.

The first approach was taken by *Sojka et al.* [1989], who confronted Dynamics Explorer 1 (DE 1) images of the aurora with DE 2 in-situ measurements of auroral precipitation data. *Sojka et al.* created a time-dependent model of electron energy flux and characteristic energy by simultaneous measurements of intensity at two wavelengths. A similar approach allowed *Rees et al.* [1988] to present a case study of electron energy flux, electron characteristic energy, and Pedersen and Hall conductances derived from multi-spectral DE 1 imaging of the aurora. This inversion method is presently hindered by problems such as low dynamic range of the signal, large wavelength bandwidth of the detector, albedo background radiation, uncertainties in off-nadir normalization of intensities, and various theoretical uncertainties. Ground and airborne investigations do not fare better, as they show poor agreement between themselves, with satellite measurements, and with model predictions [Rees et al., 1989].

In order to study the average characteristics of high-latitude auroral emissions at various levels of magnetic activity, one must acquire a large database and employ some

averaging scheme to it. This is the approach taken by this study. The purpose is (1) to create a statistical model of Far Ultraviolet (FUV) auroral emissions and (2) to relate this model to a statistical model of particle precipitation into the high-latitude ionosphere. The first objective is to create a model that is neither a mathematical representation [Holzworth *et al.*, 1975; Meng *et al.*, 1977] nor an instantaneous 'snapshot' of the auroral oval [Sojka *et al.*, 1989]. The empirical model is to delineate the average position and intensity of the auroral oval and other emissions of the high-latitude region at various levels of magnetic activity. The second objective is to associate the average electron energy and energy flux to various features of the emission, such as the nightside and dayside auroral oval, the polar cap, and the cusp.

The empirical model presented here was derived from several hundred 1356Å images of the aurora borealis obtained by Polar BEAR at solar minimum. Maps of the aurora were sorted by the ground-based activity index K_p and related to similar maps of precipitating electron characteristics.

The auroral oval is one of the most pronounced manifestations of the interaction of the solar wind with the earth's magnetic field. The concept of the auroral oval was derived from early ground-based investigations of the global auroral distribution (see Feldstein and Galperin [1985] and references therein). Major advantages this work has over previous optical investigations of global auroral intensity [Feldstein and Starkov, 1970; Sandford, 1968; Shepherd, 1979] is the large field-of-view of the space-borne imaging instrument, the automatic processing of hundreds of images, and the fact that we can include daylight aurora. Also the relatively small bandwidth of the detector (36Å) implies that we are looking mainly at single emitting species (atomic oxygen) when the precipitating electrons are cold.

Several studies in the past deduced global characteristics of precipitating electrons

using large data sets from satellite-borne particle detectors [*Spiro et al.*, 1982; *Hardy et al.*, 1985; *Fuller-Rowell and Evans*, 1987]. Fluxes, energies, and conductances were determined at various levels of geomagnetic activity in elements of a spatial grid in corrected geomagnetic coordinates. Here we use the global electron precipitation patterns of *Hardy et al.* [1985,1987].

Section 2 discusses technical characteristics of the spacecraft, imager, and detector, data selection, and interplanetary conditions when available. We describe the image processing, binning and averaging of the data, and the precipitation data used in this study in section 3. Section 4 presents and discusses the average auroral intensity maps at five levels of magnetic activity ($K_p = 0-4$). Auroral emissions are associated with characteristics of the precipitating electrons in the nightside and dayside auroral oval, the polar cap, and cusp. Finally we conclude by comparing our results with previous empirical investigations of the high-latitude ionosphere in section 5.

3 INSTRUMENTATION

Technical characteristics of the spacecraft (Polar BEAR), imager (AIRS), and detectors were previously described by *Schenkel et al.* [1986] and *DelGreco et al.* [1988]. A brief summary of the important features of the instrument relevant to this study follows. Interplanetary Magnetic Field (IMF) conditions for the data set chosen for this study are described when available.

Polar BEAR was launched at the end of 1986 to a nearly circular orbit at an altitude of approximately 1000 kilometers. The orbit was nearly polar (inclination angle 89.56°) and non sun-synchronous. The line of sight of AIRS was reflected by a mirror. Each pixel was equivalent to a mirror step with an integration time of 6.83 milliseconds. The far

ultraviolet instantaneous field of view was $0.373^\circ \times 1.53^\circ$ parallel and perpendicular to the scan direction, respectively. AIRS provided 326 samples of emission count in an angular scan from -65.2° to $+65.2^\circ$ perpendicular to the satellite orbit. The mirror scan cycle, which was completed in three seconds, produced a single raw image line. A typical station pass with eleven minute recording time provided ~ 220 scan lines spaced according to the forward motion of the spacecraft. Data was collected by the instrument and transmitted immediately to the receiving station in range.

AIRS acquired a single scene per receiving station pass along the orbit in four separate wavelength bands. Most of the useful images were acquired at the Far Ultraviolet (FUV) band centered on 1356\AA with detector number 2. This study utilizes images from this band and detector only. The Full Width at Half Maximum (FWHM) of this FUV window was 36\AA . There are two emitting species of importance in the 1356\AA bandpass: atomic oxygen and molecular nitrogen. The atomic oxygen doublet is $^3P_2 - ^5S_2$ at 1355.5\AA and $^3P_1 - ^5S_2$ at 1358.5\AA . The principal molecular nitrogen LBH band within the bandpass is from the $a^1\Pi_g$ state (3,0) at 1353.7\AA . The relative contribution of the two species to the measured intensity depends on the energy spectrum of the precipitating electrons and the look direction.

The sensitivities of the detectors were derived from preflight calibrations in a vacuum chamber [Schenkel *et al.*, 1986]. The sensitivity of the second detector in laboratory conditions at 1356\AA was 61 Rayleighs per count in the counting period [DelGreco *et al.*, personal communication; 1989]. (One Rayleigh is $10^6 \text{ photons cm}^{-2} \text{ s}^{-1}$ for 4π steradians). It is assumed here that the sensitivity of the second detector at 1356\AA was constant at the pre-launch values during January to February 1987. The system dark count per pixel integration time was less than 1 for all channels. Thus, the principal noise is the statistical fluctuations of the signal.

The data set for this study comprised of 378 FUV (1356Å, FWHM 36Å) images of the aurora, obtained between January 21, 1987, and March 1, 1987. The images were sorted according to K_p , because statistics for IMF binning were poor. 136 images had concurrent IMP 8 measurements of the IMF and solar wind speed. The interplanetary data were obtained from the National Space Science Data Center data base [Couzens and King, 1989]. Solar wind and IMF parameters are quoted for a 1-hour time lag between the hourly averaged interplanetary data and image acquisition time [Baker *et al.*, 1983; Brautigam *et al.*, 1991]. IMF conditions (in geocentric solar magnetospheric coordinates) were as follows: $B_z < 0$ for 91.2%, $B_y > 0$ for 87.5%, and $B_x > 0$ for 58.8% of the 136 images. Solar wind speed varied from 348 to 632 km s⁻¹ with an average of 465 km s⁻¹.

4 DATA ANALYSIS

Algorithms for Polar BEAR image processing were described in detail in the past [Oznovich *et al.*, 1991]. An outline of the geometric mapping and radiometric corrections applied to the images is given in subsection 1. In order to produce maps of average intensity, the FUV images were binned according to corrected geomagnetic latitude, magnetic local time, and magnetic activity. Hereafter we refer to a pixel as the basic element in an image, and to a bin as the basic element in an averaged map. We describe the binning and averaging of the data, the uncertainty in the average rate of emission of each bin, and the smoothing procedure applied to the resultant maps in subsection 2. One of the main thrusts of this work is to identify the average energy and energy flux of auroral electrons that excite the observed FUV emissions. Subsection 3 describes the source of precipitation data used in this study, and discusses our intensity sensitivity in terms of sensitivity to characteristics of the precipitating particles.

4.1 Image Processing

Geometric rectifications to the image included transformations from the satellite coordinate system to a reference system, from the reference system to the geographic coordinate system, and from the geographic system to the corrected geomagnetic coordinate system. Position in the corrected geomagnetic coordinate system is given by two parameters - Corrected Geomagnetic Latitude (CGL) and Magnetic Local Time (MLT). This coordinate system was based on the first six terms in the spherical harmonic development of the potential following the dipole term [*Hakura, 1965; Gustafsson, 1969*]. A dipole correction was added to the corrected geomagnetic latitude for an assumed auroral altitude of 120 kilometers. A further correction to CGL, due to diurnal and seasonal variations of the dipole tilt angle, will be discussed later. The dipole tilt angle is the angle between the direction of the sun and the direction of the north magnetic dipole pole (relative to the center of the earth).

Radiometric corrections included speckle noise removal, background airglow subtraction, and off-nadir normalization of auroral intensities. Subtraction of dayglow intensities from the image was based on theoretical calculations of the dayglow column brightness. Given a model atmosphere and volume emission rates, integration of the emission along an arbitrary look direction considering absorption processes was performed. The resultant column brightness was convolved with the instrument response to produce the theoretical dayglow count rate. The expected signal was linearly fit to the observed signal at all dayglow pixels, thereby creating a theoretical airglow image that best fits the observations. This theoretical image was subtracted from the photometrically raw image to produce a net auroral image.

Our images were obtained during two months at winter solstice and minimum solar activity. Consequently, the model atmosphere used is the MSIS-86 (Mass Spectrome-

ter/Incoherent Scatter) model atmosphere [Hedin, 1987] (hereafter *M86*) with the following parameters: geographic latitude 70° , geographic longitude 0° , local time 0.0 hours, day 40, daily $F_{10.7}$ and its 3-month average 70, and a magnetic activity index $A_p = 9.0$. These parameter values are typical for these data. The volume production rates of Strickland *et al.* [1983] for the dayglow emissions in the 1356\AA band were used after scaling to our model atmosphere.

Normalization of measured auroral intensities to nadir was based on the expected ratio of theoretical off-nadir auroral intensities to nadir intensities. These line-of-sight integrations used auroral volume emission rates of the *M86* atmosphere, calculated by an updated auroral electron code [Strickland, personal communication, 1991]. An incident Maxwellian electron spectrum with characteristic energy of 1.5 keV was assumed for this normalization only. As shown by Oznovich *et al.* [1991], this energy (1.5 keV) minimizes the uncertainty in off-nadir normalization for incident electrons with characteristic energies in the range of 0.1 keV to 5 keV. At the maximum look direction (55° to nadir), the uncertainty is approximately 30% for incident electrons with the above energies.

4.2 Binning and Smoothing of the Data

The 378 auroral images chosen for this study were sorted to five levels of magnetic activity ($K_p = 0, 1, 2, 3$, and 4). There were 21, 104, 149, 70, and 34 images in each K_p level, respectively. Images were plotted in a polar projection of the CGL-MLT coordinate system. Intensities were averaged in 35 divisions of CGL (from 55° to 90° , each division 1° long), and in 48 divisions of MLT (each division half an hour wide). The averaging of intensities within a single bin typically consisted of hundreds of pixels for the $K_p = 0$ and 4 maps and thousands of pixels for the $K_p = 1, 2$, and 3 maps.

The total coverage of the northern hemisphere in a given map is determined by the

combined field-of-view of the images that contribute to that map. A full coverage of the northern geomagnetic hemisphere above 55° is not obtained by any of our five maps. Gaps in the data in CGL-MLT space are most pronounced near dawn and dusk, where they can reach CGL 73° .

It has been claimed [Whalen, 1985] that distributions of average auroral parameters can produce values of intensity that never occur in nature, since instances of nonoccurrence of aurora within a spatial interval (considered to carry a zero intensity) are averaged together with cases of finite intensity within that interval. The averaging technique employed here excludes such cases. The intensity in a pixel is added to the computation of the average bin intensity in the final map only when the pixel is in the current image field-of-view, and is an auroral one, i.e. carries a nonzero value.

Oznovich *et al.* [1992] showed that the latitude of the auroral oval varies with the Dipole Tilt Angle (DTA), and gave a simple empirical equation for the latitudinal shift as a function of MLT. Figure 1 shows a cross-section along the noon-midnight meridian of the $K_p = 0$ map. The dashed line is for raw count rates (not corrected for DTA). The continuous line is for data corrected for a DTA of 90° . There are two effects to this correction. The first is that auroral emissions near local noon (midnight) are shifted poleward (equatorward) by $0-3^\circ$. This is due to the fact that our data exhibits DTA values of $85^\circ-120^\circ$, almost always higher than the selected 90° normalization angle. The second effect is that the latitudinal scatter of auroral emissions in the averaged maps is reduced by $1-2^\circ$. The FWHM of the latitudinal profile of the raw nightside (dayside) count rate shown in Figure 1 is 7° (10°). In contrast, the FWHM of the DTA-corrected nightside (dayside) data is 5° (8°).

The following factors contribute to the uncertainty in the average rate of emission of each bin: (1) Statistical fluctuations of the signal, which are proportional to the square

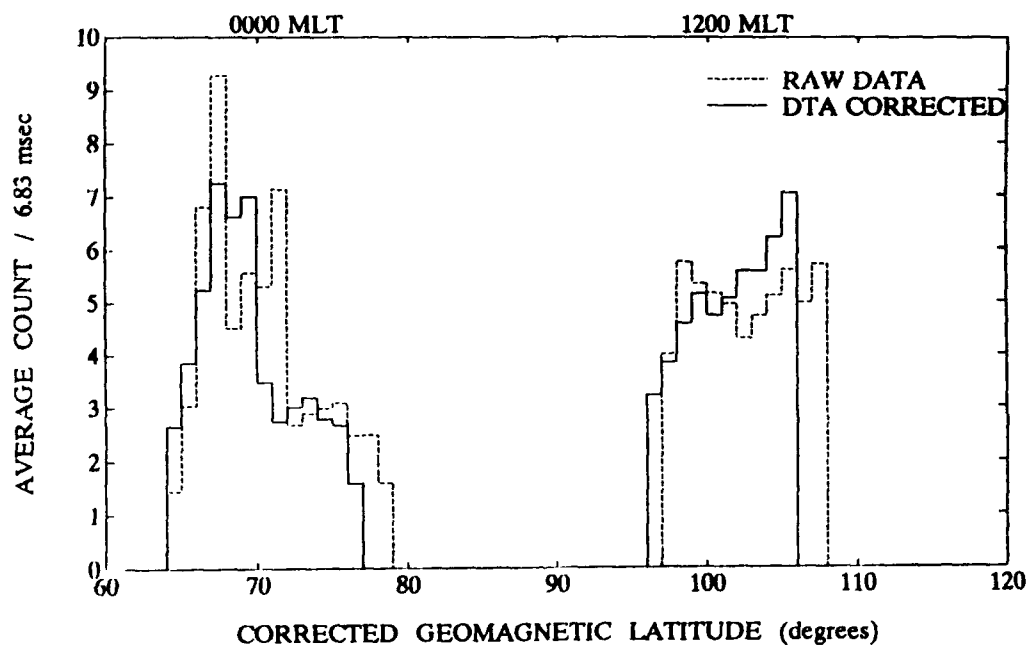


Figure 1: A cross-section of the $K_p = 0$ map (Fig. 4a) of average auroral intensity at 1356\AA along the noon-midnight meridian. The dashed line is for raw count rates (not corrected for dipole tilt angle). The continuous line is for data corrected for a dipole tilt angle of 90° . The standard deviation of bin intensity is discussed in section 3 and Figure 2.

root of the signal; (2) Uncertainty in the normalization of pixel intensity to nadir, as discussed above; (3) Averaging of continuous auroral emissions with radiation from discrete arcs within a single bin; (4) Averaging images by the 3-hour K_p index, which poorly reflects the response of auroral precipitation to solar wind-magnetosphere interactions [Brautigam *et al.*, 1991]. The ratio of the standard deviation of count rates within an individual bin to the bin average count rate is shown in Figure 2 for the $K_p = 0$ (a) and $K_p = 4$ (b) maps. Other K_p maps exhibit intermediate values. The variations in count rates within an individual bin increase with magnetic activity. For the $K_p = 0$ map (Fig. 2a), the standard deviation is mostly 30–60% of the average count rate. The standard deviation increases to 150% of the average count rate for the $K_p = 4$ map (Fig. 2b). The scatter is most significant around midnight, where discrete arcs are numerous, and least significant in the dawn and dusk sectors. This is in partial agreement with Spiro *et al.* [1982], who found that the smallest relative variations in the energy flux of auroral electrons within a given bin occur between 0200 and 0900 MLT. In order to reduce the uncertainty effects of individual bin intensities, the 35×48 maps were smoothed by a 3×3 median filter. At the lowest latitude ($55\text{--}56^\circ$) the median operator was applied to six spatial bins.

4.3 Electron Precipitation Maps

The global electron precipitation patterns of Hardy *et al.* [1985,1987] were deduced from integrals of electron spectra from the F2 and F4 satellites of the Defense Meteorological Satellite Program (DMSP) and the P78-1 spacecraft of the Space Test Program. Approximately 19,000 northern and southern hemisphere passes of the spacecrafts from the late 1970s were used to produce average electron spectra from 50 eV to 20 keV. Details on the satellites and detectors can be found in Hardy *et al.* [1979,1985]. Hardy *et al.* [1987] fitted the latitudinal profiles of the base 10 logarithm of the electron integral number flux and

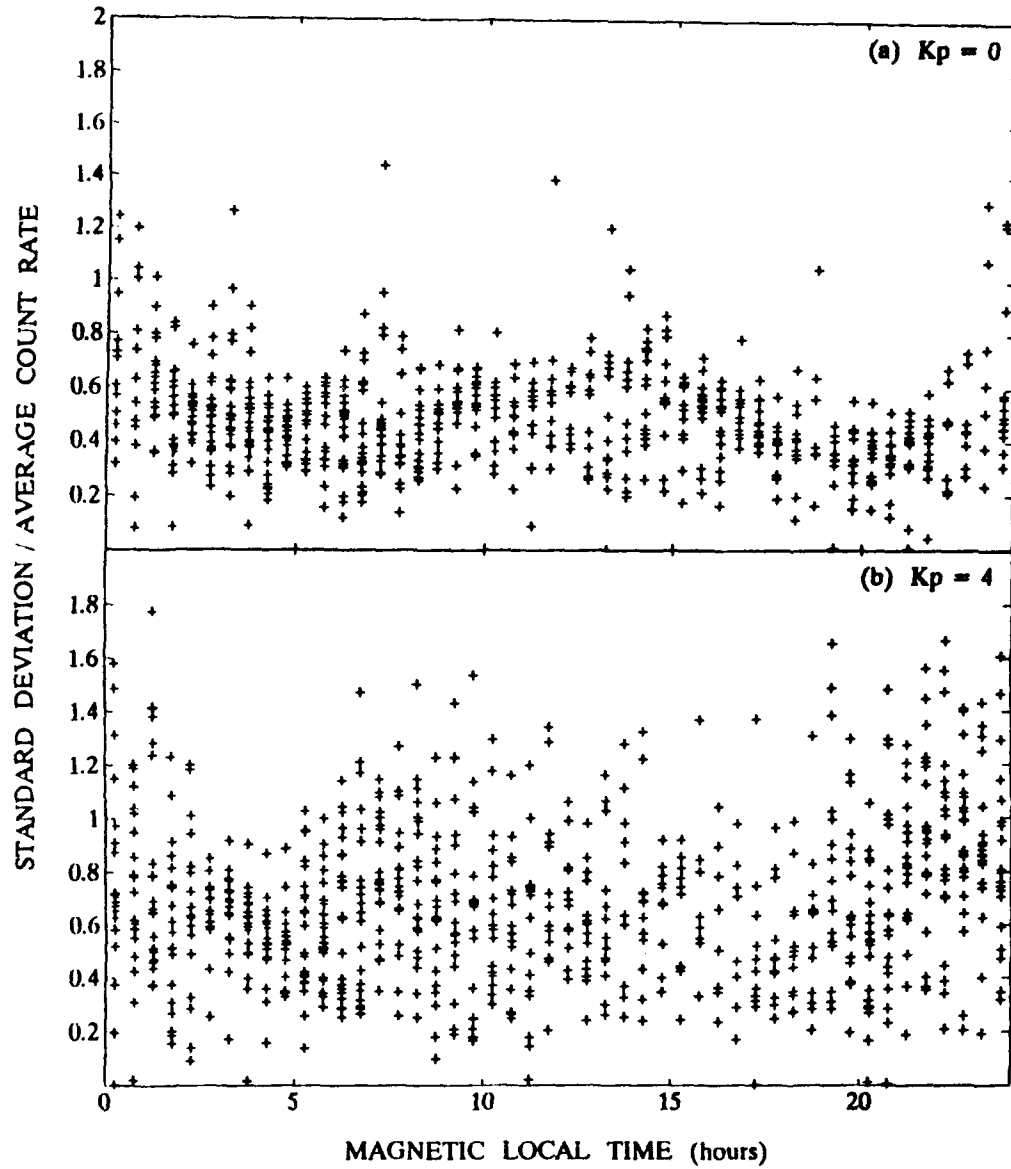


Figure 2: Ratio of the standard deviation of count rates within an individual map bin to the average count rate within the bin for the $K_p = 0$ (a) and $K_p = 4$ (b) maps.

integral energy flux of *Hardy et al.* [1985] (hereafter *H85*) for each half-hour-long MLT sector to an Epstein function [Booker, 1977]. The MLT dependence of the four coefficients of their Epstein function was fitted by a seventh-order Fourier series. We reconstructed maps of electron number flux and energy flux for our spatial grid using their method and coefficients, and derived maps of average electron energy by dividing the energy flux by the number flux for our five cases of K_p .

In comparing detected auroral emissions with characteristics of the precipitating particles, it is important to note implications of intensity detection level on particles one is sensitive to, in terms of average energy and energy flux. Figure 3 shows a scatter plot of the electron average energy and energy flux from our reconstructed *H85* maps for $K_p = 0-4$. The continuous (dashed) line characterizes incident auroral electrons with Maxwellian (Gaussian) spectra that produce a count of 1 in the second detector of AIRS. The theoretical lines were calculated by the procedure described above for characteristic electron energies of 100 eV to 10 keV for the *M86* atmosphere. The average energy is twice the characteristic energy for a Maxwellian distribution, and equals to the characteristic energy for a Gaussian distribution. Note that our data is sensitive to most of the precipitation at latitudes higher than 55° . At low average energies (less than 1 keV), the 61 Rayleighs intensity detection threshold translates to an energy flux threshold of approximately $0.1 \text{ ergs cm}^{-2} \text{ s}^{-1}$.

5 MAPS OF AVERAGE AURORAL INTENSITY

This section presents and discusses northern hemisphere maps of the average auroral intensity at 1356\AA . The maps are shown in Figure 4a–4e for five levels of magnetic activity ($K_p = 0-4$, respectively). The zigzag border in Figure 4a–4e is the overall field-of-view

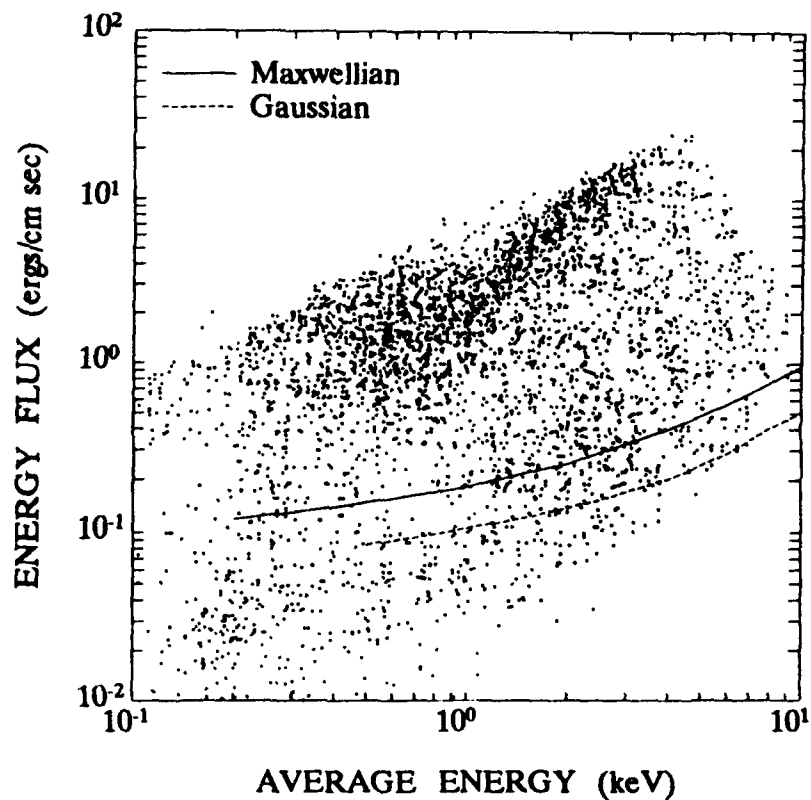


Figure 3: A scatter plot of electron average energy and energy flux for $K_p = 0-4$ reconstructed from *Hardy et al.* [1985,1987]. The continuous (dashed) line characterizes incident auroral electrons with Maxwellian (Gaussian) spectra that produce a count of 1 in the second detector of AIRS at 1356\AA . The theoretical lines were calculated by an updated auroral electron code [*Strickland*, personal communication, 1991].

of the corresponding map. The discussion on auroral emission morphology and characteristics of the precipitating particles associated with it is divided to three subsections: nightside auroral oval, dayside auroral oval, and polar cap and cusp. Emissions from the auroral oval are confined to a belt (that becomes more circular as magnetic activity increases) whose center is shifted several degrees midnight of the geomagnetic pole. As will be shown, the spatial distribution, magnetic activity dependence, and characteristics of the precipitating electrons of the nightside and dayside parts of the oval differ markedly. Figure 4a displays the familiar keyhole shape of the polar cap, which turns to a roughly circular disk at active periods (Fig. 4e). The distinction between the auroral oval and polar cap is far from clear-cut. In the discussion to follow polar-cap emissions (and the lack thereof) are considered as those arising approximately from latitudes higher than 80° . An effort to identify cusp emissions is treated within the context of the polar cap.

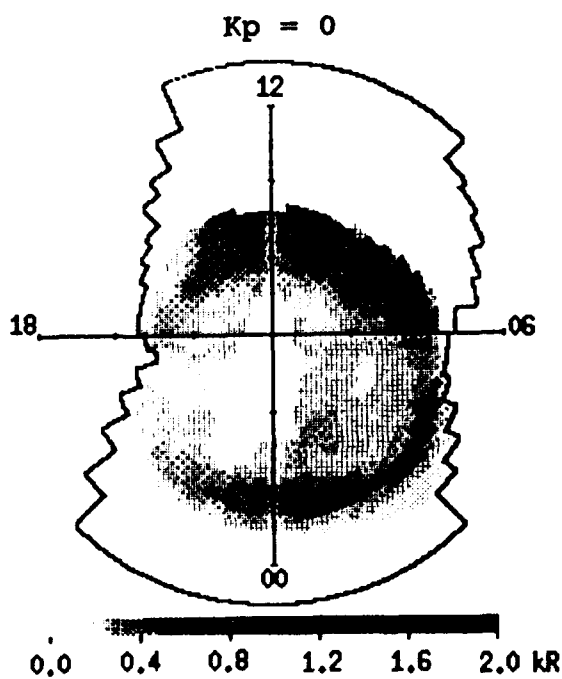


Fig. 4a

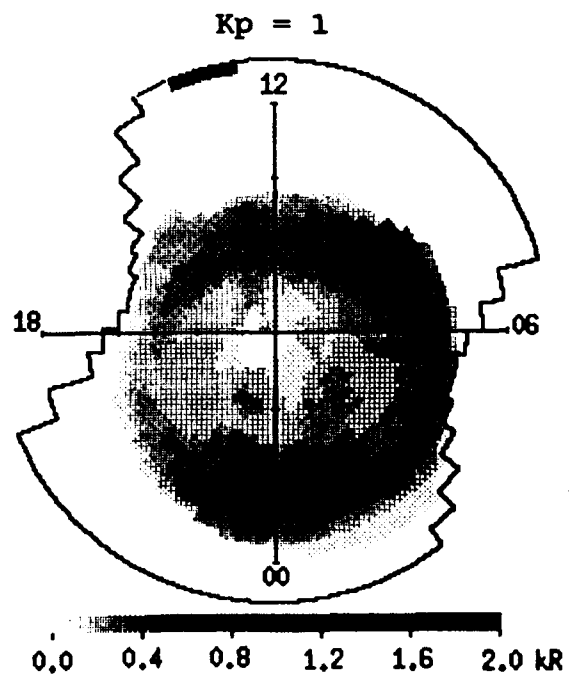


Fig. 4b

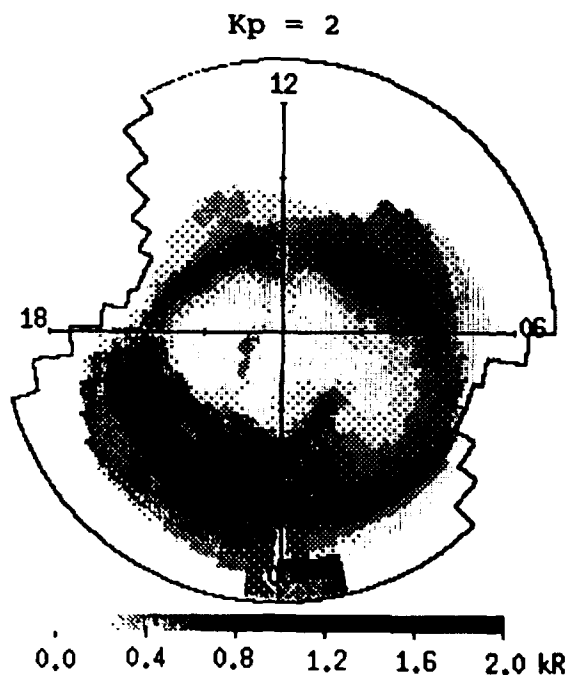


Fig. 4c

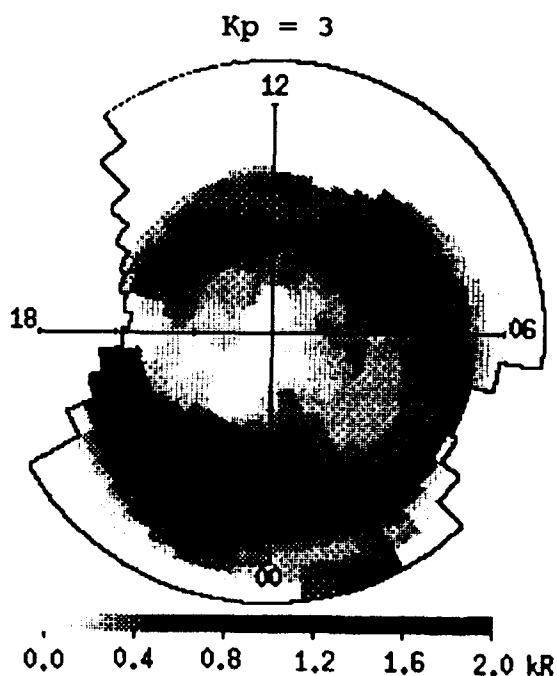


Fig. 4d

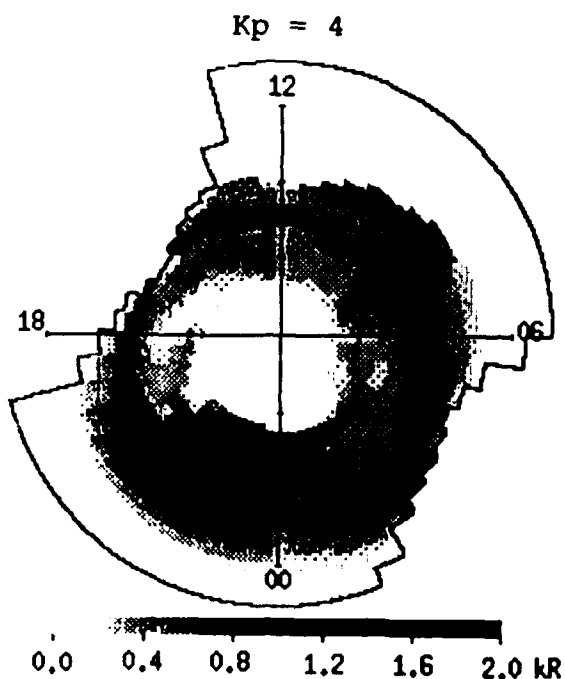


Fig. 4e

Figure 4: Maps of average auroral intensity at 1356\AA in corrected geomagnetic coordinates. Maps a, b, c, d, and e are for $K_p = 0, 1, 2, 3$, and 4, respectively. Tic marks label CGL 60° , 70° , and 80° . The zigzag border is the overall field-of-view of the corresponding map.

5.1 Nightside Auroral Oval

The nightside part of the FUV auroral oval is roughly symmetric about the noon-midnight meridian for $K_p = 0$ and roughly symmetric about a meridian 1–2 hours prior to midnight for other K_p values. A single maximum in the average intensity can be found between 1800 and 0600 MLT. It is located near midnight. Table 1 identifies the maximum intensity (in kilo-Rayleighs) in CGL and MLT for each K_p level. The average electron energy and energy flux are identified for that maximum from the *H85* maps.

All of the following parameters increase monotonically with magnetic activity in the nightside oval: maximum FUV intensity, latitude of peak emission, and width of the oval. As the level of magnetic activity increases, the maximum intensity increases from 0.4 to 1.5 kR and is shifted from 69° to 76° CGL. The latitudinal extent of the emissions varies with magnetic local time and activity. In general it is largest at local midnight and increases with K_p . The nightside maximum near local midnight is also the overall maximum intensity for all K_p values but 0. This is in accordance with the MLT dependence of the energy flux. The FWHM of auroral intensity at midnight is 5° at $K_p = 0$ and 9° at $K_p = 4$. In contrast, the FWHM of the average energy at midnight is 8° at $K_p = 0$ and 15° at $K_p = 4$, and that of the energy flux is 7° for both cases of K_p . The contribution of discrete arcs to the total emission from the oval also increases with magnetic activity. This change transforms a relatively uniform oval at quiet periods to a highly structured one at active periods.

Auroral oval precipitation is traditionally attributed to hot ($\bar{E} > 1$ keV) electrons. The maximum average energy in the nightside oval is 3–4 keV for $K_p = 0$ –4. However, the 1356Å emission is more sensitive to cold ($\bar{E} \leq 1$ keV) than to hot electrons. This could be gained theoretically from the lines of Figure 3 and experimentally from Table 1. The average electron energy of the peak nightside FUV emission in Table 1 is ~ 1 keV.

K _p	Maximum	Average	Energy	CGL	MLT
	Intensity	Energy*	Flux*		
	kR	keV	ergs cm ⁻² s ⁻¹	degrees	hours
<i>night</i>					
0	0.43	1.15	0.45	68-69	0000-0030
1	0.51	0.86	0.36	72-73	2300-2330
2	0.71	1.65	1.39	69-70	2230-2300
3	0.95	1.22	0.49	73-74	2230-2300
4	1.55	1.00	0.17	75-76	0000-0030
<i>morning</i>					
0	0.45	0.51	0.36	75-76	0800-0830
1	0.46	0.54	0.42	74-75	0730-0800
2	0.48	0.29	0.46	76-77	0800-0830
3	0.56	0.74	0.89	73-74	0800-0830
4	0.74	1.32	1.59	70-71	0700-0730
<i>afternoon</i>					
0	0.38	0.26	0.30	79-80	1400-1430
1	0.42	0.33	0.39	78-79	1430-1500
2	0.50	0.49	0.53	77-78	1500-1530
3	0.60	0.83	0.81	72-73	1600-1630
4	0.71	0.23	0.28	72-73	1430-1500

Table 1: Maximum average intensity of auroral oval emissions from the maps shown in Figure 4a-4e.

*Electron precipitation data were reconstructed from *Hardy et al.* [1985,1987].

In principal, auroral emissions should vary linearly with the energy flux. In reality, the peak FUV intensity coincides with the peak energy flux only for the lowest level of magnetic activity ($K_p = 0$, approximately at 69° CGL, 0000 MLT). At increasing levels of magnetic activity, the peak intensity shifts poleward and the peak energy flux shifts equatorward. The energy flux of the peak FUV emission increases from 0.5 to $1.4 \text{ ergs cm}^{-2} \text{ s}^{-1}$ for K_p values of 0–2, then drops to $0.2 \text{ ergs cm}^{-2} \text{ s}^{-1}$ for $K_p = 4$. This is in contrast to a monotonically increasing maximum energy flux in the electron precipitation maps: from $0.5 \text{ ergs cm}^{-2} \text{ s}^{-1}$ for $K_p = 0$ to $3.9 \text{ ergs cm}^{-2} \text{ s}^{-1}$ for $K_p = 4$.

5.2 Dayside Auroral Oval

The dayside part of the oval is roughly symmetric about the noon-midnight meridian for all K_p levels but 4. The relative contribution of discrete arcs to the total dayside emission is greatest for the most active map (Fig. 4e), and, as in the case of the nightside oval, creates a highly structured oval. It should be noted that even with the smoothing algorithm described in the previous section, the low statistics at our extreme K_p levels (21 and 34 images for Figures 4a and 4e, respectively) contributes to fluctuations in the average intensity.

Two maxima in the average 1356\AA intensity are apparent in the dayside part of the oval: one in the morning (0600–1200 MLT) and one in the afternoon (1200–1800 MLT). Table 1 identifies the location of these maxima in CGL-MLT coordinates, and lists its average electron energy and energy flux. In choosing the two maxima, abrupt changes in the latitude of peak intensity between adjacent MLT sectors are ignored as due to residual noise in the data.

The peak FUV intensity increases monotonically with magnetic activity in both the morning and afternoon. In both cases the latitude of peak emission decreases with mag-

netic activity. The morning emissions are typically 2–4° equatorward of the afternoon emissions. Consequently, if one were to fit circles to the maximum emission, they would be centered 1–2 hours past midnight.

The latitudinal extent of the dayside emissions increases with magnetic activity. The FWHM of auroral intensity at 0800 (1500) MLT is 9° (10°) for $K_p = 0$ and 15° (6°) for $K_p = 4$. In contrast, the FWHM of the average energy at 0800 (1500) MLT is 9° (3°) for $K_p = 0$ and 8° (4°) for $K_p = 4$, and that of the energy flux is 10° (9°) for $K_p = 0$ and 7° (6°) for $K_p = 4$.

Emissions from the dayside auroral oval are due to electrons that are colder than the corresponding nightside electrons. At both morning and afternoon, the peak intensity is associated with cold ($\bar{E} \leq 0.8$ keV) electrons (with the exception of $K_p = 4$ at 0700 MLT). Maximum average energies in prenoon sectors are much higher (3–6 keV) than the average energies associated with peak emission. Peak average energies are typically 3–5° equatorward of peak emissions in the FUV.

The relation of auroral intensities to electron energy fluxes conforms to traditional wisdom better in the dayside than in the nightside. As the peak intensity increases with magnetic activity, so does the energy flux in the morning and afternoon (with the exception of $K_p = 4$ in the afternoon). Energy fluxes associated with peak emission are slightly lower in the afternoon than in the morning. Peak emissions all over the oval are associated with fluxes that are lower than $1 \text{ ergs cm}^{-2} \text{ s}^{-1}$. The two exceptions are $K_p = 2$ at 2300 MLT ($1.4 \text{ ergs cm}^{-2} \text{ s}^{-1}$) and $K_p = 4$ at 0730 MLT ($1.6 \text{ ergs cm}^{-2} \text{ s}^{-1}$). These are surprisingly low fluxes given the expected linearity between emission rates and energy fluxes, and the fact that fluxes of several to tens of $\text{ergs cm}^{-2} \text{ s}^{-1}$ are found in other spatial bins of the CGL-MLT space.

5.3 Polar Cap and Cusp

There are no consistent maxima in the emissions originating from the polar cap ($\text{CGL} > 80^\circ$). The relatively narrow arcs that appear in single images are distributed almost all over the cap, thus forming a continuous region of emission in the averaging scheme employed here. In general, auroral arcs are most frequent at moderate levels of activity ($K_p = 1-3$) and in the dawn and dusk sectors.

Table 2 lists the average intensity of polar cap auroral emissions. The average electron energy and energy flux of those high latitude bins that are associated with auroral emissions were derived from the *H85* maps. The average intensity increases slowly with magnetic activity in the polar cap, similar to the K_p dependence of oval maxima. Polar cap emissions are associated with very cold electrons ($\bar{E} = 0.3-0.4$ keV) whose average energy is approximately constant for $K_p = 0-4$. Energy fluxes associated with the FUV emissions are very low (~ 0.1 ergs cm $^{-2}$ s $^{-1}$) and are also approximately constant for all K_p values.

Note that the average energy and energy flux associated with polar cap auroral emissions are at or below our detection threshold, as shown by the theoretical Maxwellian curve of Figure 3. Theoretically, we should not have detected most of these emissions, or detected them at most at the 1-count level. The intensities of Table 2 show average counts of 2-4 in the counting period. This discrepancy between our measurements and the theoretical predictions for low average electron energies will be treated more fully in the future.

The cusp is characterized by electrons that penetrate into the ionosphere directly from the magnetosheath on open field lines. Consequently the cusp is populated by a large number of very cold electrons ($\bar{E} \leq 0.2$ keV). *Hardy et al.* [1985] identified a minimum in the average electron energy near noon. This minimum was located at the poleward edge

K_p	Average	Average	Energy
	Intensity	Energy*	Flux*
	kR	keV	$ergs\ cm^{-2}\ s^{-1}$
0	0.15 (0.05)	0.33 (0.09)	0.11 (0.04)
1	0.15 (0.05)	0.42 (0.22)	0.10 (0.03)
2	0.18 (0.06)	0.32 (0.07)	0.09 (0.03)
3	0.20 (0.05)	0.42 (0.15)	0.10 (0.04)
4	0.24 (0.09)	0.29 (0.06)	0.07 (0.02)

Table 2: Average intensity of polar cap auroral emissions (CGL $> 80^\circ$) from the maps shown in Figure 4a–4e. Values in parenthesis are one standard deviation.

*Electron precipitation data were reconstructed from *Woods et al. [1985,1987]*.

of a maximum in the number flux.

Figure 5 shows the average electron energy (a), electron number flux (b), and FUV auroral intensity (c) in the dayside for $K_p = 2$. The plot is a Mercator projection of the corrected geomagnetic coordinate system for CGL $75\text{--}85^\circ$ and 0600–1800 MLT. Isocontours of average energy are plotted at 0.15, 0.2, 0.3, 0.4, and 0.6 keV. Isocontours of number flux are plotted at 1, 3, 5, 7, and $9 \cdot 10^8\ el\ cm^{-2}\ s^{-1}$. Isocontours of intensity are plotted at 0.2, 0.3, 0.4, and 0.47 kilo-Rayleighs.

The morning and afternoon maxima of the FUV emissions discussed in the previous subsection are well illustrated by Figure 5c. The shape of the emission near noon is in the form of a saddle - increasing from noon toward dawn and dusk, and decreasing from CGL $78\text{--}80^\circ$ poleward and equatorward. This is the so-called “midday gap”, which was termed as such by less sensitive imaging studies of the aurora [*Dandekar et al., 1978*]. The saddle, located approximately at 78° CGL, 1130 MLT (for $K_p = 2$), coincides with

the minimum in average electron energy and with the number flux maximum. Therefore it can be identified with the cusp. The emissions from the cusp are weak. The average cusp intensity is 0.3, 0.35, and 0.4 kilo-Rayleighs for $K_p = 1, 2$, and 3, respectively. The minimum of intensity at noon could not be identified for the $K_p = 0$ and 4 maps, probably due to their poor statistics.

6 DISCUSSION AND CONCLUSIONS

This study presented maps of average 1356Å auroral intensity for five levels of geomagnetic activity ($K_p = 0, 1, 2, 3$, and 4). It was shown that emissions from the auroral oval are confined to a belt whose center is shifted several degrees midnight of the geomagnetic pole. As magnetic activity increases, the belt expands and becomes more circular. The expansion is accompanied by an increase in the width of the oval, most notably around midnight. Polar cap arcs are most frequent at moderate levels of activity ($K_p = 1-3$) at dawn and dusk.

The peak oval intensity is located near midnight for all K_p values but 0. Two secondary maxima in the average 1356Å intensity are found in the dayside part of the oval: one in the morning and one in the afternoon. The peak nightside, morning, and afternoon intensity increase monotonically with magnetic activity. The latitude of peak emission increases with K_p at night and decreases in the dayside. The latitudinal extent of the oval is largest at or near the intensity peaks and increases with magnetic activity. The contribution of discrete arcs to the total emission from the oval also increases with magnetic activity.

A comparison of average 1356Å auroral intensities with characteristics of the precipitating electrons at various levels of magnetic activity was performed. It was shown (Fig. 3) that our 61 Rayleighs intensity threshold detection translates to an energy flux threshold of approximately $0.1 \text{ ergs cm}^{-2} \text{ s}^{-1}$ for low average electron energies (less than 1 keV).

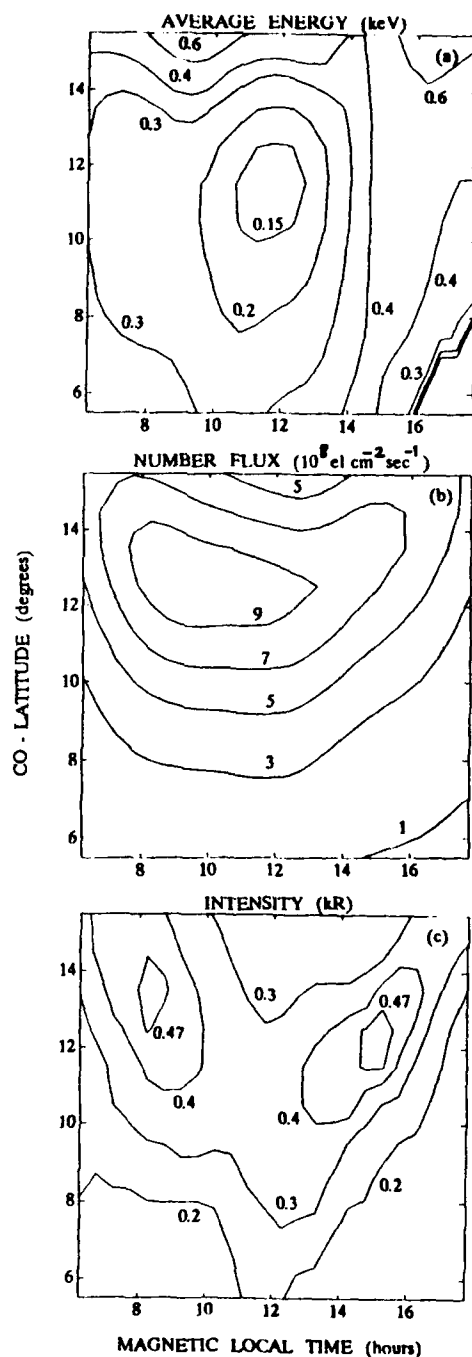


Figure 5: Average electron energy (a), electron number flux (b), and 1356Å auroral intensity (c) in the dayside for $K_p = 2$ in CGL-MLT coordinates. Isocontours of average energy are plotted at 0.15, 0.2, 0.3, 0.4, and 0.6 keV. Isocontours of number flux are plotted at 1, 3, 5, 7, and $9 \cdot 10^8 \text{ el cm}^{-2} \text{ s}^{-1}$. Isocontours of intensity are plotted at 0.2, 0.3, 0.4, and 0.47 kilo-Rayleighs.

The cumulative data shown in Figure 3 show a relationship between the energy flux and the average energy of electron precipitation leading to auroral emissions. The linear coefficient of correlation of the logarithm of the energy flux Q (in $\text{ergs cm}^{-2} \text{s}^{-1}$) and the logarithm of the average energy \bar{E} (in keV) shown in Fig. 3 is 0.84. The power law relationship between Q and \bar{E} is best fit by $Q \propto \bar{E}^{1.72}$. Using the theory of single particle motion in the presence of a magnetic field-aligned electric field, *Christensen et al.* [1987] derived an approximate expression relating the energy flux of the precipitating electrons over discrete aurora and the average particle energy: $Q \propto \bar{E}^\gamma$, where $1.5 \leq \gamma \leq 2$.

The average electron energy associated with the peak 1356Å oval emission is 0.8–1.7 keV at night, 0.3–0.7 keV in the morning (except at $K_p = 4$), and 0.2–0.5 keV in the afternoon (except at $K_p = 3$). There is no simple empirical relation between average intensity and average electron energy. Polar cap emissions are associated with very cold electrons ($\bar{E} = 0.3\text{--}0.4$ keV) whose average energy is approximately constant for $K_p = 0\text{--}4$. *Chakrabarti* [1980] deduced a characteristic energy of the precipitating particles producing polar cap emissions of 0.2–0.4 keV based on auroral intensity ratios in the 800–1400Å wavelength range. If one assumes a Maxwellian spectra for the precipitating electrons, the corresponding average energies are 0.4–0.8 keV, somewhat higher than our results for the polar cap emissions (0.3–0.4 keV).

The electron energy flux associated with the peak oval emission increases with magnetic activity in the morning and afternoon, but not so at night. It is below $0.5 \text{ ergs cm}^{-2} \text{s}^{-1}$ at night for all K_p values but 2. In contrast, the electron energy flux associated with the peak emission climbs from 0.4 to $1.6 \text{ ergs cm}^{-2} \text{s}^{-1}$ for $K_p = 0$ to 4 in the morning and from 0.25 to $0.8 \text{ ergs cm}^{-2} \text{s}^{-1}$ for $K_p = 0$ to 3 in the afternoon. At increasing levels of magnetic activity, the peak nightside (dayside) intensity shifts poleward (equatorward) and the peak energy flux shifts equatorward (equatorward).

Energy fluxes associated with FUV cap emissions are very low ($\sim 0.1 \text{ ergs cm}^{-2} \text{ s}^{-1}$) and are approximately constant for all K_p values. The shape of the emission near noon is in the form of a saddle - increasing from noon toward dawn and dusk, and decreasing from CGL 78–80° poleward and equatorward. The saddle coincides with the minimum average electron energy and maximum electron number flux associated with cusp precipitation. The average intensity of the 1356Å emission from the cusp is 0.3–0.4 kR.

7 SUMMARY AND FUTURE DIRECTIONS

Here a summary of the research during the entire project period is given. Highlights of the new advances and techniques in ionospheric remote sensing are listed, and new physical results described. Future directions in image processing, ionospheric remote sensing, and aurora research are described.

More than 400 scenes obtained by the Atmospheric/Ionospheric Remote Sensor (AIRS) aboard the Polar BEAR spacecraft were geometrically corrected and processed for airglow radiation and noise subtraction in the first year of our project. The 1991 report discussed ways to relatively normalize pixel intensities to nadir, a final step in the creation of a fully-processed auroral image database.

The theoretical off-nadir intensity relative to the nadir intensity for various characteristic energies of the incident auroral electrons was computed. These curves, as a function of the viewing direction, were compared with the optically-thin limit of radiation with no self and pure absorption. The theoretical column emission rates were also compared with data obtained by AIRS, taken from a cross section of the continuous aurora which lies along a constant auroral magnetic latitude.

Results show that for low characteristic energies of the incident electrons, the optical-

thin limit is a reasonable approximation for the data, hence for the relative normalization of auroral pixels with the off-nadir angle. An analysis method for the continuous aurora was offered. The method consisted of fitting of selected sections of auroral intensities to the theoretical curves, assuming a constant model atmosphere. This might allow one to calculate indirectly incident electron characteristic energies and energy content, and in the process select the best curve for the required calibration for any characteristic energy.

A statistical model of auroral intensity of good spatial resolution ($\Delta\text{CGL } 1^\circ$, $0.5 \text{ hr } \Delta\text{MLT}$) as a function of magnetic activity was created. The model was derived from our database of several hundred processed 1356\AA images of the aurora borealis obtained by Polar BEAR at solar minimum. The model of average auroral intensity was related to a statistical model of electron precipitation into the high-latitude ionosphere.

The peak intensity, its latitude, and the width of the oval were studied as a function of magnetic activity. Peak oval intensities were identified with the corresponding average electron energy and energy flux. Weak 1356\AA emissions near noon were found to coincide with the minimum average electron energy and maximum electron number flux associated with cusp precipitation. These emissions are located at the so-called "midday gap", which was termed as such by less sensitive imaging studies of the aurora.

Imaging of the ionosphere is a technique aimed to support studies of the structure and energetics of the ionosphere. This method also allows investigations of the lower thermosphere and magnetosphere indirectly. The final goal of these studies should be a complete and comprehensive theory of the ionosphere that can support realistic 'ionospheric weather' predictions. Such predictions will allow C³I users to plan in advance periods for undisturbed long-range communication.

The parameters that are sought are global electron density profiles, energy flux and average energy of the precipitating particles, and the true atmosphere in near real time.

This project advanced the theory and technique to the point where images of the ionosphere can be routinely processed to provide pure auroral images. The success of the airglow background subtraction and off-nadir normalization of auroral intensities developed here depend on realistic models of the atmosphere. Spectral studies of airglow and auroral emissions, particularly in the far and extreme ultraviolet wavelengths, of high wavelength resolution will no doubt improve these models.

Here average characteristics of particle precipitation were related to auroral emissions. Consequently we understand better the *average* response of the atmosphere to the *average* particle precipitation. For near real-time models, the *instantaneous* response to the *instantaneous* precipitation should be investigated. This will no doubt require simultaneous studies with many instruments at various output energy channels of the magnetosphere. Specifically, in-situ measurements of particle precipitation should be correlated with concurrent auroral emissions for many spacecraft passes at various levels of magnetic activity.

Acknowledgments. It is a pleasure to thank Dr. R. E. Huffman, Dr. R. W. Eastes, Dr. F. P. DelGreco, Dr. A. F. Quesada, and Dr. F. J. LeBlanc of the Air Force Geophysics Laboratory for their full cooperation and collaboration in the course of this study.

8 REFERENCES

- Baker, D. N., R. D. Zwickl, S. J. Bame, E. W. Hones, Jr., B. T. Tsurutani, E. J. Smith, and S.-I. Akasofu, An ISEE 3 high time resolution study of interplanetary parameter correlations with magnetospheric activity, *J. Geophys. Res.*, **88**, 6230, 1983.
- Booker, H. G., Fitting of multi-region ionospheric profiles of electron density by a single analytic function of height, *J. Atmos. Terr. Phys.*, **39**, 619-626, 1977.

- Brautigam, D. H., M. S. Gussenhoven, and D. A. Hardy, A statistical study on the effects of IMF B_z and solar wind speed on auroral ion and electron precipitation, *J. Geophys. Res.*, **96**, 5525-5538, 1991.
- Chakrabarti, S., Extreme and far ultraviolet emissions from the polar cap, *J. Geophys. Res.*, **91**, 8065-8072, 1986.
- Christensen, A. B., L. R. Lyons, J. H. Hecht, G. G. Sivjee, R. R. Meier, and D. J. Strickland, Magnetic field-aligned electric field acceleration and the characteristics of the optical aurora, *J. Geophys. Res.*, **92**, 6163-6167, 1987.
- Couzens, D. A, and J. A. King, Interplanetary medium data book, supplement 4, 1985-1988, *Rep. NSSDC 98-17*, Natl. Space Sc. Data Center, World Data Center A for Rockets and Satellites, Greenbelt, Md., Sept., 1989.
- Dandekar, B. S., and C. P. Pike, The midday, discrete auroral gap, *J. Geophys. Res.*, **83**, 4227, 1978.
- DelGreco, F. P., R. E. Huffman, J. C. Larrabee, R. W. Eastes, F. J. LeBlanc, and C.-I. Meng, Organizing and utilizing the imaging and spectral data from Polar BEAR, *Ultraviolet Technology, Proc. SPIE*, 1988.
- Feldstein, Y. I., and Starkov, G. V., The auroral oval and the boundary of closed field lines of geomagnetic field, *Planet. Space Sci.*, **18**, 501, 1970.
- Feldstein, Y. I., and Galperin, Yu. I., The auroral luminosity structure in the high-latitude upper atmosphere: its dynamics and relationship to the large-scale structure of the earth's magnetosphere, *Rev. Geophys.*, **23**, 217, 1985.

- Fuller-Rowell, T. J., and D. S. Evans, Height-integrated Pedersen and Hall conductivity patterns inferred from the TIRSOS-NOAA satellite data, *J. Geophys. Res.*, **92**, 7606-7618, 1987.
- Gussenhoven, M. S., Extremely high latitude auroras, *J. Geophys. Res.*, **87**, 2401-2412, 1982.
- Hardy, D. A., M. S. Gussenhoven, and A. Huber, The precipitating electron detectors (SSJ/3) for the block 5D/flights 2-5 DMSP satellites: Calibration and data presentation, *Rep. AFGL-TR-79-0210*, Air Force Geophys. Lab., Hanscom Air Force Base, Mass., 1979. (ADA083136)
- Hardy, D. A., M. S. Gussenhoven, and E. Holeman, A statistical model of auroral electron precipitation, *J. Geophys. Res.*, **90**, 4229-4248, 1985.
- Hardy, D. A., M. S. Gussenhoven, and R. Raistrick, Statistical and functional representations of the pattern of auroral energy flux, number flux, and conductivity, *J. Geophys. Res.*, **92**, 12,275-12,294, 1987.
- Holzworth, R. H., and C.-I. Meng, Mathematical representation of the auroral oval, *Geophys. Res. Lett.*, **2**, 377, 1975.
- Meng, C.-I., R. H. Holzworth, and S.-I. Akasofu, Auroral circle - delineating the poleward boundary of the quiet auroral belt, *J. Geophys. Res.*, **82**, 164, 1977.
- Oznovich, I., A. Ravitz, M. Tur, I. Glaser, R. E. Huffman, R. W. Eastes, and A. F. Quesada, Far ultraviolet remote sensing of ionospheric emissions by Polar BEAR, *submitted for publication*, 1991.
- Oznovich, I. *et al.*, The aurora at quiet magnetospheric conditions: repeatability and dipole tilt angle dependence, *in preparation*, 1992.

- Rees, M.H., D. Lummerzheim, R. G. Roble, J. D. Winningham, J. D. Craven, and L. A. Frank, Auroral energy deposition rate, characteristic electron energy, and ionospheric parameters derived from Dynamics Explorer 1 images, *J. Geophys. Res.*, **93**, 12,841–12,860, 1988.
- Rees, M.H., D. Lummerzheim, Characteristics of auroral electron precipitation derived from optical spectroscopy, *J. Geophys. Res.*, **94**, 6799–6815, 1989.
- Sandford, B. P., Variations of auroral emissions with time, magnetic activity and the solar cycle, *J. Atmosph. Terr. Phys.*, **30**, 1921, 1968.
- Schenkel, F. W., B. S. Ogorzalek, R. R. Gardner, R. A. Hutchins, R. E. Huffman, and J. C. Larrabee, Simultaneous multi-spectral narrow band auroral imagery from space (1150Å to 6300Å), *Ultraviolet Technology, Proc. SPIE*, 687, 1986.
- Shepherd, G. G., Dayside cleft aurora and its ionospheric effects, *Rev. Geophys.*, **17**, 2017, 1979.
- Sojka, J. J., R. W. Schunk, J. D. Craven, L. A. Frank, J. Sharber, and J. D. Winningham, Modeled F region response to auroral dynamics based upon Dynamics Explorer auroral observations, *J. Geophys. Res.*, **94**, 8993–9008, 1989.
- Spiro, R. W., P. H. Reiff, and L. J. Maher, Precipitating electron energy flux and auroral zone conductances - an empirical model, *J. Geophys. Res.*, **87**, 8215–8227, 1982.
- Strickland, D. J., and D. E. Anderson, Radiation transport effects on the OI 1356Å Limb intensity profile in the dayglow, *J. Geophys. Res.*, **88**, 9260–9264, 1983.
- Whalen, J. A., The Aurora, in *Handbook of Geophysics and Space Environment*, **12**, ed. A. S. Jursa, AFGL, 1985. (ADA167000)